Supplementary Figures

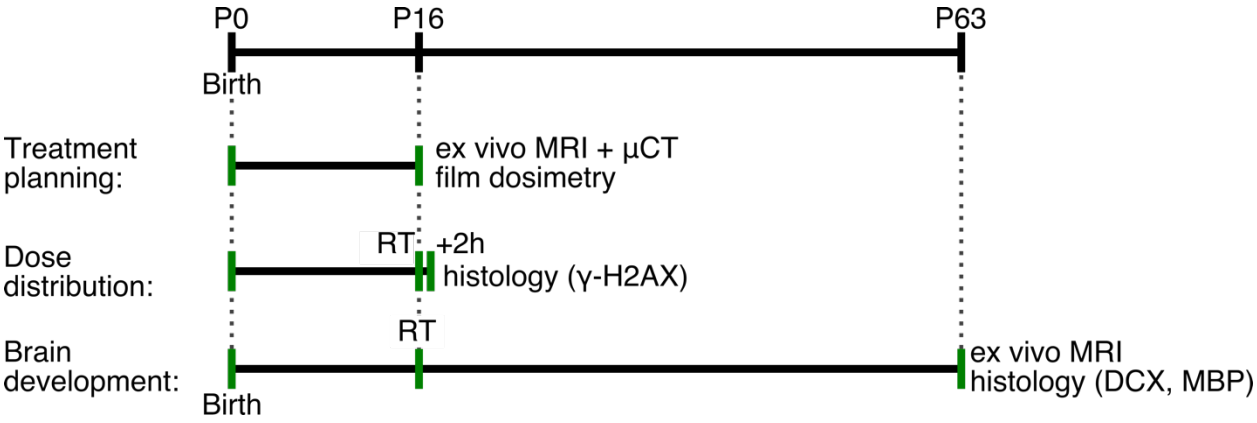

Supplementary Figure 1. The experimental timelines for each aspect of the study. MR and µCT images were used to generate a P16 atlas for radiation treatment planning. Film dosimetry in P16 brain specimens was used to confirm delivered dose. Whole-brain or focal irradiations (RT) occurred at P16, with γ-H2AX histology used to assess the spatial distribution of delivered radiation dose (using a separate group of mice 2h after RT). To assess impact of RT on brain development, ex-vivo MR images were acquired at P63, and volumetric differences computed using an automated imaging processing pipeline. In the same samples, DCX and MBP staining was used to assess neurogenesis and myelination, respectively.

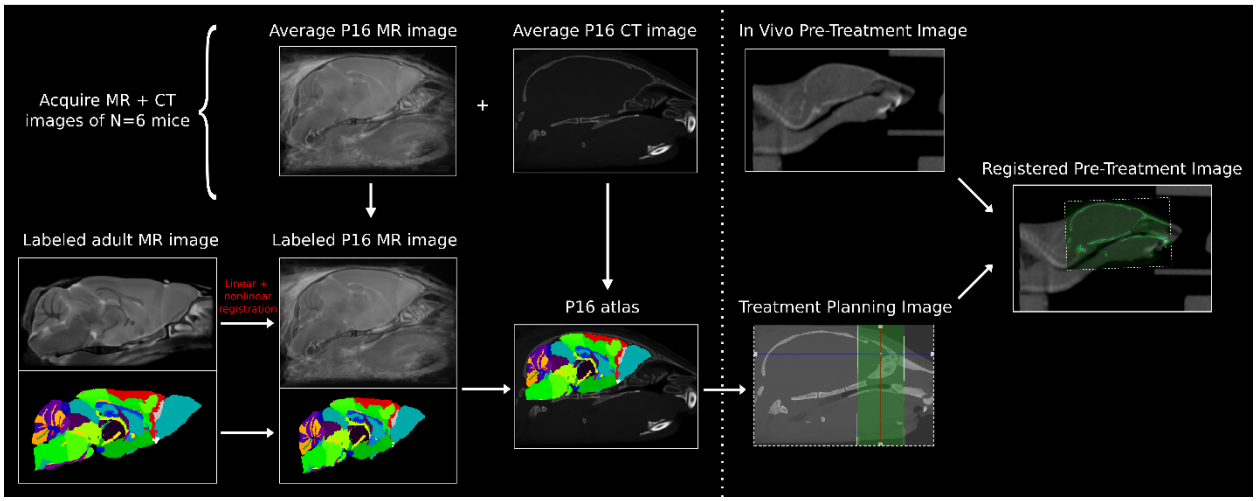

Supplementary Figure 2. The generation of a segmented P16 μ-CT atlas for planning, with registration of in vivo CT images prior to dose delivery. An ex vivo MR volume of a P63 mouse with segmented brain structures was registered linearly and nonlinearly to an average P16 ex vivo MR volume to obtain a P16 brain atlas. The P16 MR volume was then rigidly registered to the average P16 μ-CT image obtained from the same specimens to produce a P16 atlas for radiation treatment planning. This P16 atlas was used to determine the ROI coordinates for all irradiation cohorts. During each irradiation procedure, the in vivo pre-treatment image is registered to the P16 atlas and the stage position is adjusted to produce the desired treatment position.

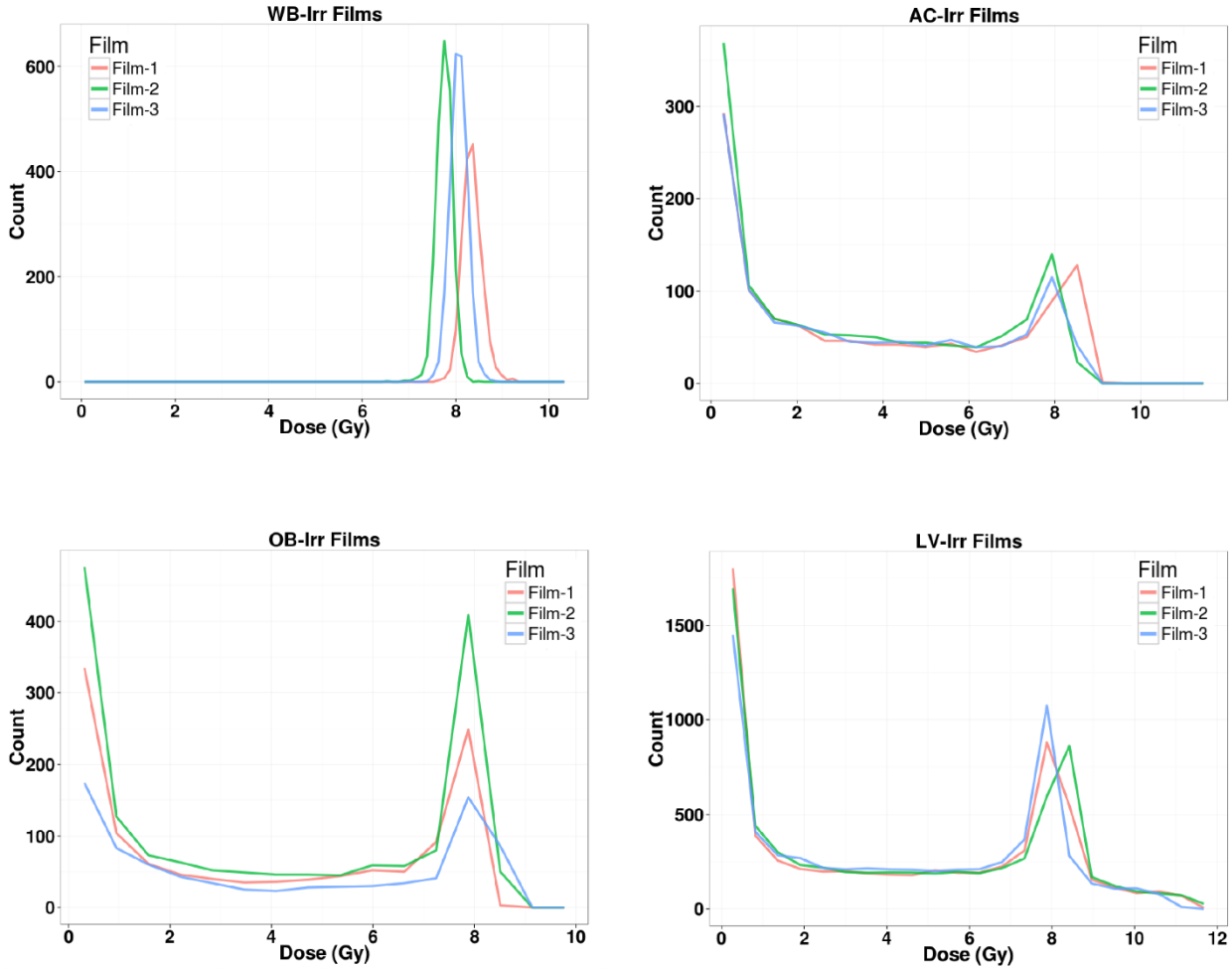

Supplementary Figure 3. Dose histograms illustrating delivered dose for each ROI as determined with radiochromic film dosimetry. EBT3 films placed within the brain and skull of ex vivo P16 specimens were treated identically to in anesthetized mice in vivo. Dose counts obtained from optical density measurements are shown as histograms (with n=3 films per irradiation ROI). The delivered dose was within ±5% error of the 8Gy target. Lower end tails in the AC-Irr, OB-Irr and LV-Irr films represent scattered dose. Higher end tails in the LV-Irr films represent regions of beam overlap due to multiple targets.

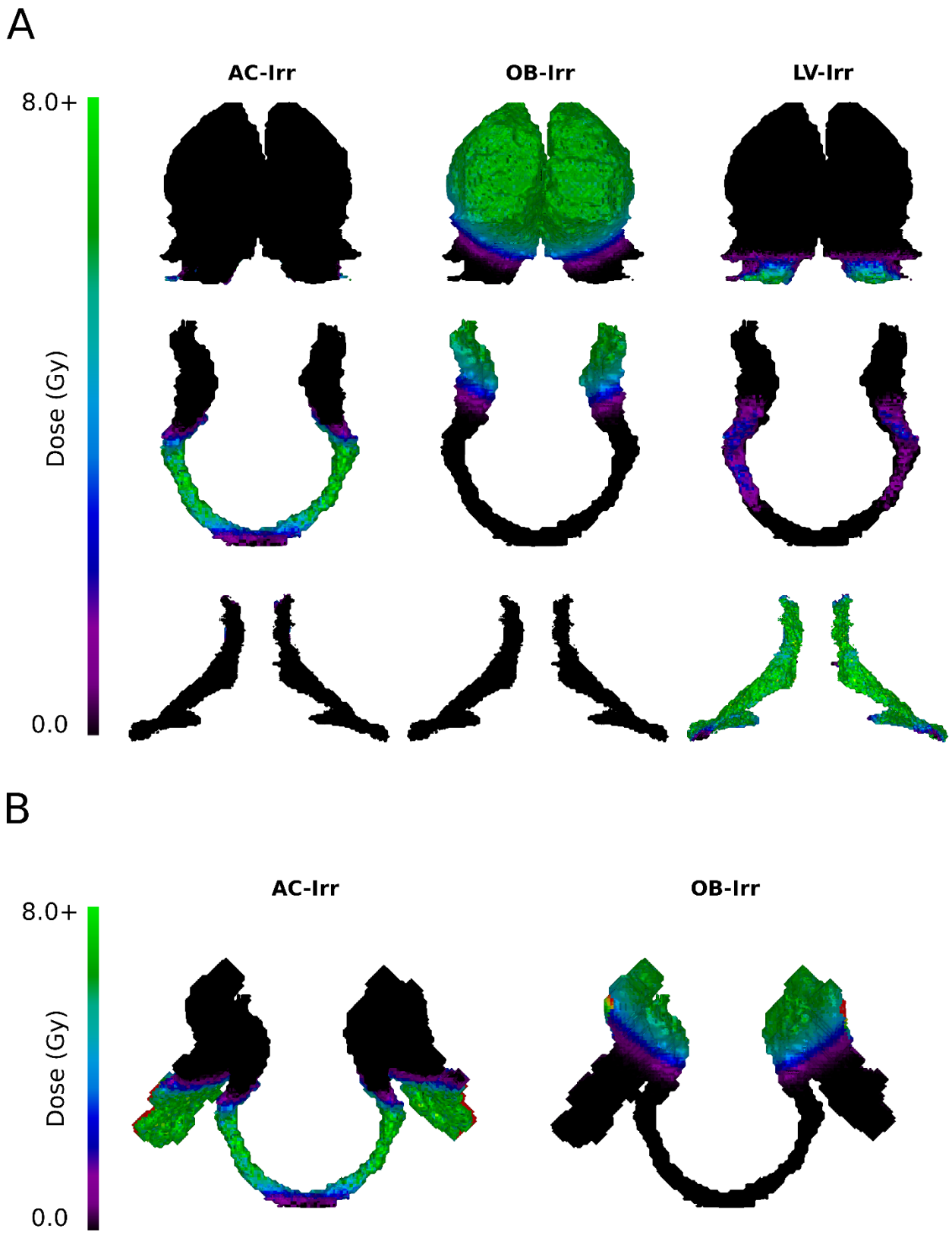
A
AC-Irr
OB-Irr
LV-Irr
8.0+
Dose (Gy)
0.0
B
AC-Irr
OB-Irr
8.0+
Dose (Gy)
0.0

Supplementary Figure 4. Horizontal views of surface renderings show simulated radiation dose distributions on targeted and untargeted brain structures. In (A), the AC-Irr, OB-Irr and LV-Irr groups are shown in columns. The delivered dose is rendered on the surfaces of the OB (top), AC (middle) and LV (bottom). In (B), the AC and LOT volumes are rendered together. The ROI sizes are not shown using a common scale.

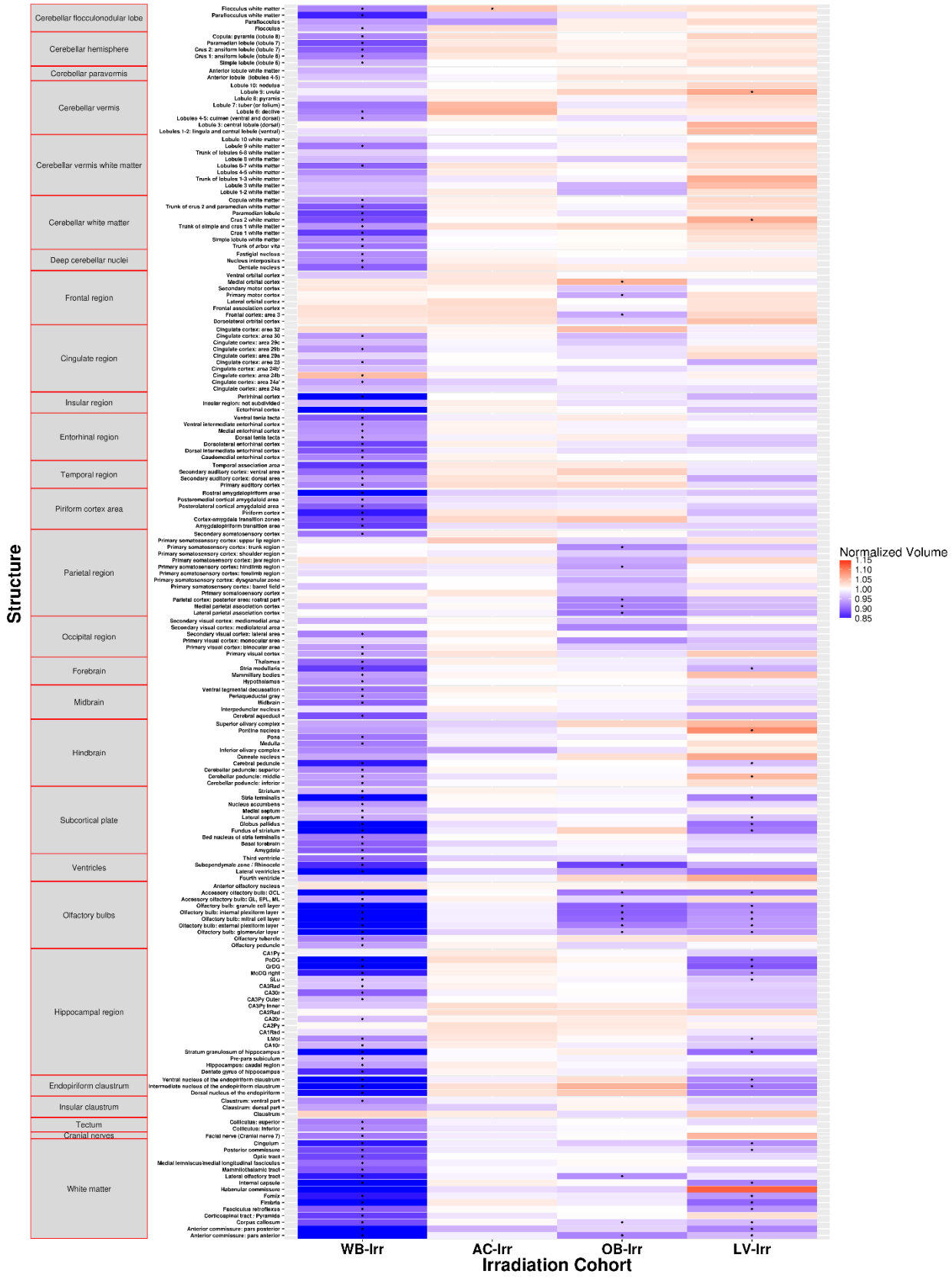
Structure
Cerebellar flocculonodular lobe
Cerebellar hemisphere
Cerebellar paravermis
Cerebellar vermis
Cerebellar vermis white matter
Cerebellar white matter
Deep cerebellar nuclei
Frontal region
Cingulate region
Insular region
Entorhinal region
Temporal region
Piriform cortex area
Parietal region
Occipital region
Forebrain
Midbrain
Hindbrain
Subcortical plate
Ventricles
Olfactory bulbs
Hippocampal region
Endopiriform claustrum
Insular claustrum
Tectum
Cranial nerves
White matter
Flocculus white matter
Paraflocculus white matter
Paraflocculus
Flocculus
Copula: pyramis (lobule 8)
Paramedian lobule (lobule 7)
Crus 2: ansiform lobule (lobule 7)
Crus 1: ansiform lobule (lobule 6)
Simple lobule (lobule 5)
Anterior lobule white matter
Anterior lobule (lobules 4-5)
Lobule 10: nodulus
Lobule 9: uvula
Lobule 8: pyramis
Lobule 7: tuber (or folium)
Lobule 6: declive
Lobules 4-5: culmen (ventral and dorsal)
Lobule 3: central lobule (dorsal)
Lobules 1-2: lingula and central lobule (ventral)
Lobule 10 white matter
Lobule 9 white matter
Trunk of lobules 6-8 white matter
Lobule 8 white matter
Lobules 6-7 white matter
Lobules 4-5 white matter
Trunk of lobules 1-3 white matter
Lobule 3 white matter
Lobule 1-2 white matter
Copula white matter
Trunk of crus 2 and paramedian white matter
Paramedian lobule
Crus 2 white matter
Trunk of simple and crus 1 white matter
Crus 1 white matter
Simple lobule white matter
Trunk of arbor vitae
Fastigial nucleus
Nucleus interpositus
Dentate nucleus
Ventral orbital cortex
Medial orbital cortex
Secondary motor cortex
Primary motor cortex
Lateral orbital cortex
Frontal association cortex
Frontal cortex: area 3
Dorsolateral orbital cortex
Cingulate cortex: area 32
Cingulate cortex: area 30
Cingulate cortex: area 29c
Cingulate cortex: area 29b
Cingulate cortex: area 29a
Cingulate cortex: area 23
Cingulate cortex: area 24b'
Cingulate cortex: area 24b
Cingulate cortex: area 24a'
Cingulate cortex: area 24a
Perirhinal cortex
Insular region: not subdivided
Ectorhinal cortex
Ventral tenia tecta
Ventral intermediate entorhinal cortex
Medial entorhinal cortex
Dorsal tenia tecta
Dorsolateral entorhinal cortex
Dorsal intermediate entorhinal cortex
Caudomedial entorhinal cortex
Temporal association area
Secondary auditory cortex: ventral area
Secondary auditory cortex: dorsal area
Primary auditory cortex
Rostral amygdalopiriform area
Posteromedial cortical amygdaloid area
Posterolateral cortical amygdaloid area
Piriform cortex
Cortex-amygdala transition zone
Amygdalopiriform transition area
Secondary somatosensory cortex
Primary somatosensory cortex: upper lip region
Primary somatosensory cortex: trunk region
Primary somatosensory cortex: shoulder region
Primary somatosensory cortex: jaw region
Primary somatosensory cortex: hindlimb region
Primary somatosensory cortex: forelimb region
Primary somatosensory cortex: dysgranular zone
Primary somatosensory cortex: barrel field
Primary somatosensory cortex
Parietal cortex: posterior area; rostral part
Medial parietal association cortex
Lateral parietal association cortex
Secondary visual cortex: mediomedial area
Secondary visual cortex: mediolateral area
Secondary visual cortex: lateral area
Primary visual cortex: monocular area
Primary visual cortex: binocular area
Primary visual cortex
Thalamus
Stria medullaris
Mammillary bodies
Hypothalamus
Ventral tegmental decussation
Periaqueductal gray
Midbrain
Interpeduncular nucleus
Cerebral aqueduct
Superior olivary complex
Pontine nucleus
Pons
Medulla
Inferior olivary complex
Cuneate nucleus
Cerebral peduncle
Cerebellar peduncle: superior
Cerebellar peduncle: middle
Cerebellar peduncle: inferior
Striatum
Stria terminalis
Nucleus accumbens
Medial septum
Lateral septum
Globus pallidus
Fundus of striatum
Bed nucleus of stria terminalis
Basal forebrain
Amygdala
Third ventricle
Subependymal zone ; Rhinocele
Lateral ventricles
Fourth ventricle
Anterior olfactory nucleus
Accessory olfactory bulb: GCL
Accessory olfactory bulb: GL, EPL, ML
Olfactory bulb: granule cell layer
Olfactory bulb: internal plexiform layer
Olfactory bulb: mitral cell layer
Olfactory bulb: external plexiform layer
Olfactory bulb: glomerular layer
Olfactory tubercle
Olfactory peduncle
CA1Py
PoDG
GrDG
MoDG right
SLu
CA3Rad
CA3or
CA3Py Outer
CA3Py Inner
CA2Rad
CA2or
CA2Py
CA1Rad
LMol
CA1or
Stratum granulosum of hippocampus
Pre-para subiculum
Hippocampus: caudal region
Dentate gyrus of hippocampus
Ventral nucleus of the endopiriform claustrum
Intermediate nucleus of the endopiriform claustrum
Dorsal nucleus of the endopiriform
Claustrum: ventral part
Claustrum: dorsal part
Claustrum
Colliculus: superior
Colliculus: inferior
Facial nerve (Cranial nerve 7)
Cingulum
Posterior commissure
Optic tract
Medial lemniscus/medial longitudinal fasciculus
Mammillothalamic tract
Lateral olfactory tract
Internal capsule
Habenular commissure
Fornix
Fimbria
Fasciculus retroflexus
Corticospinal tract : Pyramids
Corpus callosum
Anterior commissure: pars posterior
Anterior commissure: pars anterior
Normalized Volume
1.15
1.10
1.05
1.00
0.95
0.90
0.85
WB-Irr
AC-Irr
OB-Irr
LV-Irr
Irradiation Cohort

Supplementary Figure 5. Heatmap indicating brain-wide changes in volume for all atlas structures. Values are shown relative to control volumes for each structure (i.e., indicating fold-change). Structures are grouped into regions as shown at left. A dot (•) indicates statistical significance at $q<0.05$ compared to controls.

Supplementary Materials and Methods

Mice

C57Bl/6J breeding pairs (The Jackson Laboratory) were housed and bred in the University Health Network Animal Resource Centre to obtain male and female offspring for all irradiation procedures and associated experiments. The day of litter birth was designated post-natal day zero (P0). Mice were maintained in a 12h light-dark cycle with access to food and water ad libitum. C57Bl/6J mice breeding pairs from the Centre for Phenogenomics in-house colony were used to generate mice for the P16 atlas and film dosimetry experiments.

Treatment planning

To generate a representative P16 image for Hounsfield Unit (HU)-based radiation treatment planning, six fixed P16 mouse heads were imaged ex vivo with μ-CT at a spatial resolution of 10 μm with a 40 kV / 250 mA beam specification (10 mW) using a Bruker SkyScan 1172 system (Bruker μ-CT, Belgium). Image HU values were calibrated to mouse bone densities obtained from two mouse bone phantoms (Bruker, Belgium). In order to map brain anatomy within the P16 μ-CT volume, ex vivo MRI was performed on the same samples. Average MR and CT images representative of the six P16 mouse brains were generated independently by registration. A segmented neuroanatomical MRI atlas was linearly and nonlinearly registered to the average P16 MR image, which was in turn affine registered to the average μ-CT image (Supplementary Figure 2). The segmented atlas was then mapped to the average μ-CT image and provided the basis for treatment planning.

Beam geometries were established based on the use of circular collimators for each ROI. Parallel-opposed beam pairs 180° apart were used in all cases with the aim of achieving a

homogeneous 8 Gy dose distribution in the ROI. WB-Irr, AC-Irr and OB-Irr plans used collimators oriented in the dorsoventral, mediolateral and dorsoventral directions, respectively. The LV-Irr plan employed three parallel-opposed beam pair targets in the mediolateral direction (with a small degree of overlap at the lateral edges of the beams).

Radiochromic film dosimetry was performed in order to quantify the dose deposited for each ROI (Supplementary Figure 3).

Histology

For γ-H2AX staining (STTARR Innovation Centre, Toronto), mice were intraperitoneally anaesthetized using ketamine (150 mg/kg) and xylazine (10 mg/kg) and transcardially perfused. Brains were dissected and paraffinized into blocks, dewaxed in xylene, and rehydrated using alcohols. Antigen retrieval was performed in a sodium citrate buffer of pH 6.0 for 8 min. Autofluorescence was reduced with a 0.1% Sudan Black B solution for 8 min. Non-specific antibody binding was blocked using 5% normal goat serum for 30 min at room temperature. Sections were incubated for 1h at room temperature with rabbit anti-γ-H2AX primary antibody (1:1500; Bethyl Laboratories Inc.), and then with goat anti-rabbit Alexafluor 555 (1:200) secondary antibody for 1h at room temperature. All antibodies were diluted using Dako antibody diluent. Sections were washed, incubated in a working solution of 4', 6-diamidino-2-phenylindole (DAPI) for 5 min, rinsed with dH_2O, and coverslipped with Vectamount hardset mounting media. Stained images were captured on a scanning laser confocal microscope (TISSUEscope 4000, Huron Technologies).

For histological analyses of myelination and neurogenesis at P63, mouse brains were dissected and cryoprotected in a 30% sucrose solution and frozen at -20°C. Coronal sections cut

at 40-μm thickness were collected in tissue cryoprotectant solution in 96-well plates, and stored at -20°C. Sections containing LVs and the hippocampus between 1.1 mm and -3.1 mm relative to the bregma were used for doublecortin (DCX), and myelin basic protein (MBP) immunohistochemistry. Primary antibodies included rabbit anti-DCX (1:1000, Abcam), and rat anti-MBP (1:200, Millipore). Secondary antibodies conjugated to Cy2 (1:200, Jackson ImmunoResearch) and Cy3 (1:200; Jackson ImmunoResearch) were used to reveal the immunoreactivity. Sections were counterstained with DAPI.

Cell Counting and MBP Staining Intensity Analysis

DCX positive (+) cells were counted within the dentate gyrus (DG) including a 50-μm hilar margin of the subgranular zone (SGZ), another neurogenic niche located within the hippocampus, using a Zeiss Imager M1 microscope with the Stereo Investigator software (MicroBrightField, Williston, VT, USA). A counting frame and sampling grid of 75 μm × 75 μm were used with a magnification of 63X, sampled every seventh section. The coefficient of error was between 0.03 and 0.06 in all stereological studies. For the SVZ, AC, and CC, a non-stereologic method was used, counting DCX^+ cells in the left and right SVZ within at least 2.13×10^7 μm^3 of SVZ in three sections at seven section intervals per mouse.